# Dynamic simulation of a solar-autothermal hybridized gasifier: Model principle, experimental validation and parametric study

Axel Curcio, Sylvain Rodat, Valéry Vuillerme, Stéphane Abanades

# Dynamic Simulation of a Solar-Autothermal Hybridized Gasifier: Model Principle, Experimental Validation and Parametric Study

**Axel Curcio [1], Sylvain Rodat [1], Valéry Vuillerme [2], Stéphane Abanades [1 *]**

[1] Processes, Materials and Solar Energy Laboratory, PROMES - CNRS,
7 rue du Four Solaire, 66120 Font-Romeu Odeillo, France

[2] Univ. Grenoble Alpes INES - CEA,
50 avenue Lac Léman, 73375 Le Bourget-du-Lac, France

* Corresponding author. Email: stephane.abanades@promes.cnrs.fr. Phone: + 33 (0)4 68 30 77 30.

## ABSTRACT

Solar thermochemical fuel production technologies, such as biomass gasification, are confronted to the intermittency of solar irradiance. The development of dynamic simulation tools is thus required to design around-the-clock control strategies. An innovative model was developed here, based on unsteady mass and energy conservation equations, considering gas-phase thermodynamic equilibrium and heterogeneous char oxidation kinetics. The accumulation of char and gas species production rates were therefore tracked throughout operation, giving insight into the reactor dynamics with optimized computational cost. The model was validated via a comparison with experimental results, regarding both thermal and chemical reactor performances. Simulations reliably predicted the evolution of reactor temperatures and syngas production rates, under both solar-only and hybridized (solar-autothermal) operation. Parametric studies regarding the impact of reactants injection rates on steady-state performances were finally proposed. Steam addition (0.22 to 0.60 g/min) increased the syngas $H_2$:CO molar ratio significantly (1.13 to 1.47). Biomass addition (1 to 3 g/min) boosted the solar-to-fuel efficiency (0.22 to 0.47), but altered the reactor temperature. Finally, oxygen addition kept the reactor running despite fluctuations of solar power, while decreasing the total $H_2$+CO production and cold-gas efficiency linearly. A constant $H_2$+CO production (2.17 NL/min) could however be achieved by feeding additional biomass and oxygen during hybridization, thus limiting the cold-gas efficiency decrease and improving the reactor energy efficiency (0.29 to 0.40). Such a dynamic reactor model can be further applied to hybridized gasification process optimization and dynamic control under real fluctuating solar irradiation conditions.

## KEYWORDS

Solar fuels; Gasification; Hybrid solar reactor; Biomass; Char; Dynamic modelling

## 1. INTRODUCTION

With the aim to develop a green path to produce renewable syngas, a mixture of $H_2$ and CO for the synthesis of liquid fuels, solar gasifiers have been developed since 1980 [1,2] to carry out the high-

temperature conversion of carbonaceous feedstocks. Conventional autothermal gasifiers use *in-situ* combustion to supply heat to the endothermal gasification reaction, leading to net feedstock losses and syngas dilution in combustion products (mainly $CO_2$ and $H_2O$) [3]. Contrarily, allothermal solar gasifiers enable high chemical efficiencies because all the feedstock can be converted into syngas (no combustion). Numerous reactor designs have already been assessed, including packed-beds, variations of fluidized-bed and spouted-bed technologies, vortex flows, and molten-salt reactors [4,5]. Fluidized beds are promising solutions to ensure a continuous and homogeneous heating of solid particles, but a char throughput must be managed due to incomplete solid conversion [6]. Spouted beds ensure long solid residence times, and efficient solid-gas transfer rates with little spouting gas requirements [7]. The application to woody biomass pyro-gasification naturally emerged for the production of a fully renewable syngas fuel [8]. In several lab-scale experiments, the storage of solar heat into fuels through biomass feedstock upgrading was demonstrated, as cold-gas efficiencies higher than 1 were reported (1.30 in [9], 1.35 in [10]). However, the upscaling towards industrial production is still compromised because of a particularly complex modelling [11] and specific technological challenges. On the one hand, optimizing the particles circulation and the temperatures in the reactor requires sophisticated 3D modelling techniques including radiative transfer [12,13]. On the other hand, optimizing the dynamics of solar gasification through the day requires strong assumptions to reduce computational costs [14,15]. The present work responds to the second problematic, by proposing a model suitable to simulate the dynamic control of a solar gasifier.

Indeed, coping with the daily fluctuations of solar power for continuous processing still requires further research work [16]. Yearly solar reactor efficiencies are yet estimated using strong hypotheses (steady-state modelling, hourly time steps…), leading to overestimated reactor efficiencies, wrong reactor dimensioning, and approximate implementation of hybridization strategies [17]. In this context, thermodynamic equilibrium modelling is often employed to assess both autothermal and allothermal gasification mechanisms [18]. As only the initial elemental composition of the chemical system is required, it is a convenient and fast alternative to including chemical kinetics [19]. Good agreements can be achieved regarding syngas ($H_2$, CO and $CO_2$) production rates, as well as low-temperature (800 °C) char residuals [20]. However, using thermodynamic equilibrium does not enable to describe the dynamics of char oxidation, which rule the accumulation of solid particles throughout operation [21]. The present study aims at improving thermodynamic equilibrium modelling, by considering heterogeneous kinetics of char oxidation and thus describing more accurately the gasifier transients with reasonable computational cost.

This new method is applied to the pyro-gasification of beech wood, in a hybrid solar-autothermal spouted-bed reactor [13,22,23]. The ideal reaction of wood gasification is provided in Equation 3. However, the actual mechanism comprises the pyrolysis and devolatilization of wood feedstock followed by the gasification of the solid char product [24]. Methane reforming (Equation 1) and Water-Gas Shift (WGS, Equation 2) reactions rule the distribution of gaseous species during their stay in the cavity. Besides, the *in-situ* injection of oxygen enables to heat the reactor chamber [25–28], despite an altered syngas quality. During such autothermal hybridization, steam and wood injection rates can be tuned to control the syngas quantity and quality [29]. However, the assessment of more sophisticated hybridization strategies (simultaneous control of the three reactants injection rates) cannot be carried out without an efficient dynamic simulation tool.

$$CH_4 + H_2O_{(v)} \longrightarrow CO + 3\ H_2 \qquad \Delta H° = +206.1\ kJ/mol \qquad (1)$$

$$H_2O_{(v)} + CO \leftrightarrow H_2 + CO_2 \qquad \Delta H° = -41.1\ kJ/mol \qquad (2)$$

$$CH_{1.45}O_{0.65} + 0.35\ H_2O_{(v)} \longrightarrow CO + 1.07\ H_2 \qquad \Delta H° = +106.3\ kJ/mol \qquad (3)$$

A new dynamic model of a solar hybrid gasification reactor was developed and experimentally validated in this work. To date, such dynamic modelling for the control and operation of hybrid solar gasification systems has not been considered. The model is based on unsteady mass and energy conservation equations, combined with heterogeneous char oxidation kinetics while considering gas-phase thermodynamic equilibrium. It is robust and flexible-enough for application to wide operating conditions and reactor scales. It features a cavity receiver where the gaseous phase is assumed to be at thermodynamic equilibrium. Meanwhile, the oxidation of solid char (by $O_2$, $H_2O$ and $CO_2$) is ruled by heterogeneous kinetics featuring Random-Pore Modelling (RPM, [30]). This chemical scheme is coupled to a detailed thermal model, featuring distinct temperatures for the reactor solid parts and the gas phase. The resulting code enables to simulate the main dynamics of woody biomass gasification, under both solar heating and *in-situ* oxy-combustion. Reasonable computing times are achieved, making the code compatible with annual dynamic simulation and continuous reactor control. After this model overview, a set of experimental validation cases was examined to verify thermal responses and chemical products outcomes. Dynamic simulation revealed a satisfying agreement with the observed thermal and chemical responses of the reactor under both solar and solar-autothermal hybridized operations. Finally, a complete parametric analysis was performed to determine the impact of reactants injection rates (steam, biomass, oxygen) on reactor temperatures, char accumulation, and chemical efficiencies. Such a dynamic model is particularly well suited for an application to reactor optimization and dynamic control. It can be further applied for performance and environmental impact assessments of solar gasification plants under real fluctuating solar irradiation conditions.

# 2. MATERIAL AND METHODS

## 2.1. Solar reactor design

The simulation code was conceived to model the operation of a lab-scale spouted-bed solar gasification reactor [22] (Figure 1). Figure 1-a shows the whole reactor casing, topped by a hemispherical glass window. It is set at the focal point of a 1.5 kW beam-down solar furnace. A 1.15 L hopper contains feedstock, that is provided to the cavity through a screw driver. Figure 1-b shows the 0.24 L conical cavity, made of a high-resistant, 3 mm thick FeCrAl alloy. It is surrounded by an insulation layer of 25 mm minimal thickness. Above the cavity, an alumina cap is set with a 20 mm wide aperture, to let sunlight enter while minimizing radiative losses. The cap is covered by two 2 mm thick layers of zirconia felts, which restrict the aperture diameter (~18 mm) to limit thermal losses. Biomass is injected in the upper half of the cavity, and solid particles are continuously stirred thanks to a jet of oxidizing gases ($H_2O$, $O_2$) and argon coming from the lower injection nozzle. The produced syngas is recovered through an alumina tube while outlet Venturi pumping is used to limit overpressure (the cavity pressure is usually maintained around 0.87 bar, the atmospheric pressure at laboratory location being 0.85 bar).

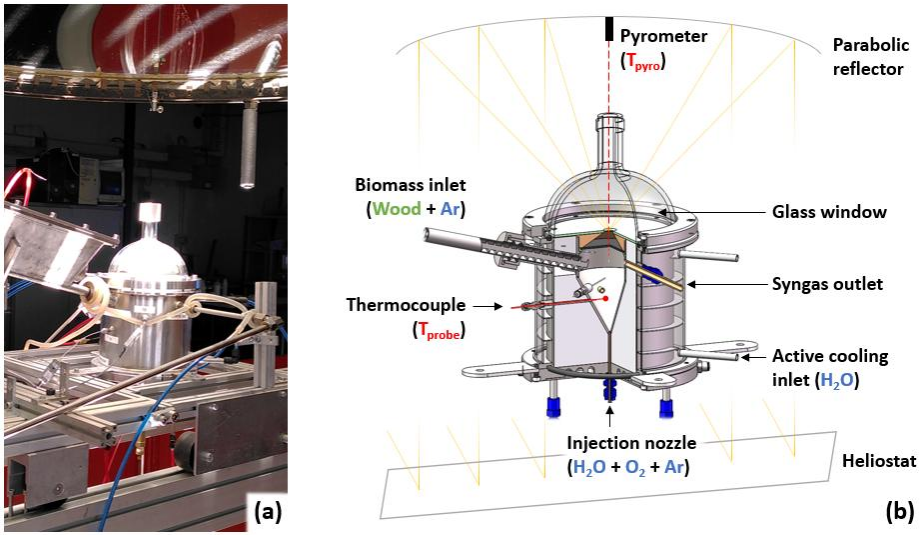


**Figure 1. Experimental setup: (a) Photograph of the solar spouted-bed gasifier during operation, (b) Scheme of the gasifier and solar concentrator**

Temperatures in the cavity are measured thanks to several B-type thermocouples and a pyrometer (4.8-5.2 µm, solar-blind). In particular, one thermocouple ($T_{probe}$) is shielded in an alumina tube and inserted inside the lower half of the conical cavity. The pyrometer ($T_{pyro}$) is directed vertically towards the cavity's inside, through a $CaF_2$ window.

Raw syngas pumped out of the cavity is cooled through a 1 m long steel pipe, visible in the foreground of Figure 1-a. An ice-cooled bubbler then enables to trap steam and to capture most solid residues. Two filters finally collect the remaining solid particles, before the gas stream is analysed and vented. The mole fractions of $H_2$, CO, $CO_2$ and $CH_4$ are measured by an online analyser (GEIT GAS 3100 SYNGAS) with a sampling period of 3 seconds.

## 2.2. Usual operating conditions

Operation of the reactor can be performed under both direct and indirect heating. In indirect heating, a SiC-coated graphite emitter plate is added under the alumina cap (15 mm below the focal plane aperture). It absorbs concentrated sunlight, and heats the cavity by infra-red radiative transfer. In direct heating, sunlight directly enters the cavity and heats the conical region without any intermediate. A comparison of these two heating modes was already discussed [28], where higher $H_2$ and CO yields were observed using direct heating, during both solar-only and solar-autothermal hybrid gasification experiments.

**Table 1. Composition and heating value of beech wood biomass feedstock (dry basis)**

| Moisture [wt%] | C (dry) [wt%] | H (dry) [wt%] | O (dry) [wt%] | Ash (dry) [wt%] | HHV (dry) [kJ/g] | LHV (dry) [kJ/g] |
|---|---|---|---|---|---|---|
| 9.8 | 49.8 | 6.0 | 43.4 | 0.6 | 19.5 | 18.3 |

The solar gasification of 1.2 g/min of millimetric beech wood particles (measured characteristics given in Table 1) is usually performed thanks to a 0.2 g/min stream of water injected at the bottom of the conical region [31]. A 0.2 NL/min stream of argon is blown along with water to stir the bulk solid, and 0.5 NL/min of argon is injected in the hopper to avoid counter current heat and mass fluxes along the screw driver. An additional 2.0 NL/min argon stream is directed towards the glass window to protect it, under both direct and indirect heating modes.

## 2.3. Characteristic time analysis

Upon entering the cavity, the feedstock is dried and pyrolyzed. The pyrolysis actually starts in the hot screw driver, but no traces of pyrolysis oils or tars were ever spotted, showing that pyrolysis essentially occurs in the cavity at temperatures above 800 °C [32] and produces high yields of gases. The solid char particles then undergo heterogeneous oxidation by oxygen (partial combustion), steam or $CO_2$ (gasification). The characteristic times for prevailing mechanisms are provided in Table 2, considering the reactor temperatures observed with CFD [26] (drying and pyrolysis at 800 °C, gas reactions at 1100 °C, char oxidation at 1300 °C). The kinetics of drying and pyrolysis are taken from [33], where they were validated for beech wood particles with granulometries in the range 315-450 µm and 1120-1250 µm. As for the char oxidation kinetics, taken from [34], they were determined over char particles of 44 µm average diameter. They were still successfully used to simulate the gasification of larger particles (coal particles of diameters 50, 100, 200 and 500 µm in [35]), and they appear to be a reasonable choice among the kinetics proposed in the literature [36].

**Table 2. Calculation of characteristic times for the main mechanisms occurring in the gasifier**

| Reaction | Rate [$E_a$ in kJ/mol, P in MPa, C in kmol/m$^3$] | $t_{characteristic}$ [s] | $t_{residence}$ [s] | Source |
|---|---|---|---|---|
| Drying | $dm_{H2O}/dt = -5.0\cdot10^{8} \exp(-50/RT) \times m_{H2O}$ | $5.4\cdot10^{-7}$ | | [33] |
| Pyrolysis | $dm_{wood}/dt = -7.4\cdot10^{4} \exp(-70/RT) \times m_{wood}$ | $3.5\cdot10^{-2}$ | | [33] |
| $C + O_2$ | $dX_C/dt = +1.36\cdot10^{6} \exp(-130/RT) \times P_{O2}^{0.68} \times f(X_C, \Psi=14)$ | $3.8\cdot10^{-1}$ | $3.9\cdot10^{-1}$ | [34] |
| $C + H_2O$ | $dX_C/dt = +2.45\cdot10^{7} \exp(-214/RT) \times P_{H2O}^{0.86} \times f(X_C, \Psi=3)$ | $3.1\cdot10^{+1}$ | $5.9\cdot10^{+1}$ | [34] |
| $C + CO_2$ | $dX_C/dt = +6.78\cdot10^{4} \exp(-163/RT) \times P_{CO2}^{0.73} \times f(X_C, \Psi=3)$ | $1.2\cdot10^{+2}$ | $2.3\cdot10^{+2}$ | [34] |
| WGS (f) | $dC_{H2O}/dt = -2.98\cdot10^{8} \exp(-163/RT) \times C_{H2O} \times C_{CO}$ | $3.2\cdot10^{+0}$ | | [26] |
| Methane reforming | $dC_{H2O}/dt = -1.48\cdot10^{11} \exp(-260/RT) \times C_{H2O} \times C_{CH4}$ | $3.2\cdot10^{+1}$ | | [26] |

The surface function term featured in heterogeneous kinetics is detailed in Equation 4. According to the RPM theory, the oxidation rate of a char particle evolves over time due to structural changes (increase of porosity). This effect is modelled by a function of the particle conversion $X_C$ (Equation 5), that is called surface function. A structure parameter $\Psi$ is also featured. In [34], $\Psi$ equals 14 for combustion and 3 for $H_2O$ and $CO_2$ gasification. By integrating the surface function until a 99% conversion, a residence time of char $t_{residence}$ can be proposed for the oxidation reactions, as provided in Table 2. It is almost identical to the Arrhenius-based characteristic time in the case of combustion, and it becomes much higher in the case of $H_2O$ or $CO_2$ gasification (1.9 times the $t_{characteristic}$ values).

$$f(X) = (1 - X_C)\sqrt{1 - \Psi \cdot \ln(1 - X_C)} \quad (4)$$

$$X_C(t) = \frac{m_C(t=0) - m_C(t)}{m_C(t=0)} \quad (5)$$

All characteristic times are displayed in Figure 2, on a logarithmic scale, and compared with the time step that was chosen for process simulation ($t_S$, 0.2 s). On the one hand, the drying and pyrolysis of woody biomass are fast enough to be considered instantaneous in the model. On the other hand, the

combustion of char has a characteristic time near 0.4 s, so the $t_s$ value cannot be higher than 0.2 s for a reasonable modelling of the process. A shorter time step would make calculations longer, without significantly affecting the results. $H_2O$ and $CO_2$ gasification reactions are much slower than combustion, so they will be particularly well modelled.

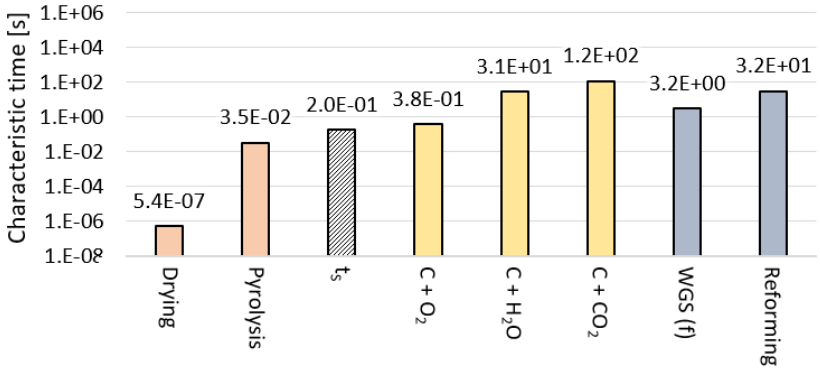


**Figure 2. Characteristic times of main mechanisms, compared with the simulation time step $t_s$**

Regarding the gas phase reactions, an average residence time can be proposed by considering the total gas output flow rate. The solar gasification of 1.2 g/min of beech wood yields a syngas flow-rate (mostly $H_2$ and CO) around 1.6 NL/min [29], added to the 2.7 NL/min of argon injected. Under steady state, and considering that the gas temperature is 1100 °C [26], the mean gas residence time therefore lies around 0.7 seconds. The comparison with WGS and reforming characteristic times (respectively 3.2 and 32 seconds) shows that syngas composition is normally ruled by kinetics, in particular regarding the production of $CH_4$.

## 2.4. Simulation code overview

The simulation code developed in this work is named DEMOSTRAR: Dynamic, Extrapolation-ready Modelling and Optimization of a Solar Thermochemical ReActoR. It is written in Python 3, using the library CANTERA [37] specialized in multiphasic thermodynamic calculations. CANTERA was already used in the literature to investigate the thermodynamic mechanisms controlling the gasification of biomass [18,38], and to identify theoretical limitations to the process. It features the thermodynamic properties of numerous species as provided by the NASA [39] and GRI-MECH [40] databases. DEMOSTRAR implements the heterogeneous kinetics of char oxidation in addition to the calculation of gas-phase thermodynamic equilibriums. Thus, the quantity of char present in the reactor at each time step can be tracked, which is not the case with only thermodynamic equilibrium calculations. This advance in modelling is brought without strongly affecting the computing costs, which is a key advantage for the implementation of continuous day-night control algorithms [15,41].

A zero-dimensional description of the cavity is proposed to couple the heat and mass balance equations. The metal alloy wall, as well as the emitter plate (when operating under indirect heating), are assumed having uniform temperatures ($T_{wall}$ and $T_{plate}$). Regarding the reactor inner volume, char particles and gases are heated by both radiative heat transfer (absorbed by char, $H_2O_{(g)}$ and $CO_{2(g)}$), and convective transfer with the walls.

As a result, the model requires around 1 minute to compute 100 minutes of operation, on a dedicated calculation machine.

The main model assumptions are summed up below:

a) The pressure in the reactor is perfectly controlled.
b) Solid parts of the reactor have uniform temperatures.

c) The gas volume is perfectly stirred (homogeneous temperatures and concentrations).
d) The gas phase only contains Ar, $H_2O$, $O_2$, $H_2$, CO, $CO_2$, $CH_4$ and $C_2H_2$ species.
e) The gas phase is considered at thermodynamic equilibrium.
f) No tars nor pyrolysis oils are modelled (due to high operation temperatures).
g) Solid char particles and gases share the same temperature.
h) Solid char particles are evenly dispersed in the reaction chamber.
i) No solid particles are entrained at the reactor outlet.

## 2.5. Thermal model

Both direct and indirect heating modes were implemented. The main modes of heat transfer considered are detailed in Figure 3. Thermal losses are dispatched between the radiative losses occurring through the upper aperture ($Q_{loss,aperture}$), the radiative losses occurring at the alumina cap upper side despite the zirconia cover felt ($Q_{loss,cap}$), and the conductive losses occurring through the reactor insulation ($Q_{loss,insul}$). The physical properties of the reactor solid parts are summed up in Table 3.

**Table 3. Thermal properties of the reactor solid parts (1000 °C)**

| | m [kg] | $\rho$ [kg/m$^3$] | $c_P$ [J/kg·K] | k [W/m·K] | $\varepsilon$ [-] |
|---|---|---|---|---|---|
| **Wall (FeCrAl alloy)** | 0.4 | 7100 | 800 | 35 | 0.7 |
| **Cap (99.7% $Al_2O_3$)** | 0.2 | 3900 | 795 | 9.1 | 0.8 |
| **Emitter plate (SiC covered Graphite)** | 0.0155 | 1400 | 710 | 25 | 0.98 |
| **Insulation (35% $SiO_2$, 65% $Al_2O_3$)** | 0.6 | 400 | 800 | 0.22 | - |

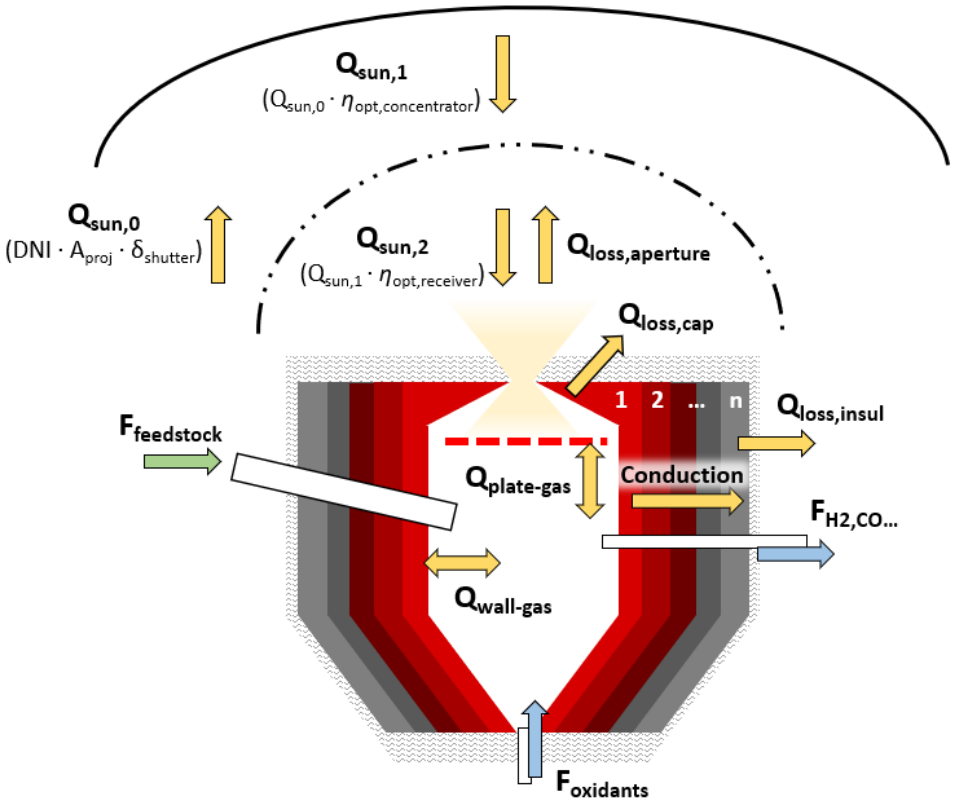


**Figure 3. Heat flows of the gasifier modelled in DEMOSTRAR**

The calculation of solar power input is detailed in Equation 6 and Equation 7. $Q_{sun,1}$ is the power delivered by the parabolic concentrator. It accounts for the losses occurring at the heliostat and at the parabolic reflector ($\eta_{opt,concentrator}$), and it can be controlled by a shutter obstructer ($\delta_{shutter}$). The value of $\eta_{opt,concentrator}$ was adjusted thanks to calorimetry measurements, so the relationship between the DNI and $Q_{sun,1}$ is well established. As for $Q_{sun,2}$, it accounts for the losses due to both the glass window and the radiation absorption by zirconia felts around the aperture due to spillage ($\eta_{opt,receiver}$). It thus corresponds to the actual solar power available at the cavity entrance.

$$Q_{sun,1} = DNI \cdot A_{proj} \cdot \delta_{shutter} \cdot \eta_{opt,concentrator} \quad (6)$$

$$Q_{sun,2} = Q_{sun,1} \cdot \eta_{opt,receiver} \quad (7)$$

The total, one-band radiative emissivity of the $H_2O$ and $CO_2$-rich gas ($\varepsilon_{gas}$) is computed using the correlation of [42] (Equation 8 and Equation 9). This correlation was established to model the heat emitted by combustion in industrial furnaces. Based on the partial pressures of both oxidants, it decreases when the gas temperature increases, consistently with conventional emissivity wide-band models. It features an effective beam length L [43,44], that differs according to the origin of radiations (walls, emitter plate, or reactor aperture). The total gas absorptivity ($\alpha_{gas}$) was taken equal to half its emissivity ($\varepsilon_{gas}$), to achieve appropriate thermal responses. Furthermore, the radiative absorptivity of the solid particles cloud ($\alpha_{char}$) is taken proportional to the projected area of particles across beam trajectories, including a correction regarding particles overlapping effects. No scattering is modelled here, because of restrictive calculation time constraints and incomplete knowledge of the char particles size distribution and optical properties. Experimental data would not enable validating such a radiation model, nor fitting an empirical law as proposed in [45]. Under this

approximation, $\alpha_{char}$ reached 3.0%, 6.0% and 11.6% for accumulated char masses equalling 0.5 g, 1 g and 2 g, respectively. The emissivity of solid particles ($\varepsilon_{char}$) was taken equal to their absorptivity.

$$\varepsilon_{gas} = 1 - e^{-\alpha_{\Sigma} PL} \quad (8)$$

$$\alpha_{\Sigma} = ((0.78 + 1.6 p_{H_2O})/\sqrt{PL} - C)\,(1 - DT) \quad (9)$$

An unsteady finite-volume conduction model was implemented to simulate the temperature distribution across the wall and insulation thickness. The alumina cap was considered to have the same temperature as the wall first layer, in accordance with CFD results [46]. The total thickness of the wall and insulant parts were 2.74 and 41.4 mm, respectively. The temperature of the inner layer enabled to compute the $Q_{cap\text{-}out}$, $Q_{wall\text{-}gas}$ and $Q_{wall\text{-}out}$ (direct heating) terms. The insulation outer area was assumed to be at 25 °C due to active water cooling (no convection is modelled).

The radiative heat transfer between the outside and the emitter plate (indirect heating) is written in Equation 10. As seen in [47], the solar power input $Q_{sun,2}$ is assumed to be entirely captured by the solid, while radiative losses are modelled by the second term. The view factor $F_{plate\text{->}out}$ gives the fraction of light emitted by the upper plate surface that reaches the aperture. It equals only 5.5%. The remaining 94.5% are transmitted towards the alumina cap. Besides, the radiative transfer between the wall and the gas + particles phase is written in Equation 11. The correction of the wall emissivity was proposed in [43], because the enclosure radiates towards itself and thus tends to behave like a black body. A constant convective heat transfer coefficient of 50 W/m²K was applied, that is a typical value for spouted beds [48]. The radiative losses attributed to the alumina cap are given in Equation 12. The first term features the cap inner area $A_{cap}$ and its view factor with the aperture (only 1.0%, thus negligible with this geometry). The second term features an apparent radiative area $A_{app}$ that is adjusted to model radiative losses occurring despite the zirconia felts covering.

$$Q_{out-plate} = Q_{sun,2} - \sigma A_{plate} F_{plate \to out} \varepsilon_{plate} \left(T_{plate}^4 - T_{out}^4\right) \quad (10)$$

$$Q_{wall-gas} = \sigma A_{wall} \frac{\varepsilon_{wall} + 1}{2} \left(\alpha_{gas} T_{wall}^4 - \varepsilon_{gas} T_{gas}^4\right) + H_{conv}(T_{wall} - T_{gas}) \quad (11)$$

$$Q_{cap-out} = \sigma A_{cap} F_{cap \to out} \varepsilon_{cap} \left(T_{wall}^4 - T_{out}^4\right) + \sigma A_{app} \left(T_{wall}^4 - T_{out}^4\right) \quad (12)$$

$$m_i c_{P_i} \frac{T_i^{t+\Delta t} - T_i^t}{\Delta t} = \sum_j Q_{j \leftrightarrow i}^{\,t+\Delta t} \quad (13)$$

Equation 13 illustrates the heat balance condition that is computed at each time step. All the heat transfer terms are expressed at the instant t+Δt instead of the instant t, according to the principle of implicit resolution. This method ensures the stability of calculations, whereas an explicit resolution scheme would impose using a much lower time step duration. The heat balances written in Equation 13 thus constitute a system of non-linear equations that is solved using Newton-like root search methods [49].

## 2.6. Chemical model

As discussed in 2.3, the feedstock drying and devolatilization are considered instantaneous upon injection. Drying is modelled using the enthalpy of vaporization of water [33]. Then, the dry feedstock particles are split into a mass of char and a mixture of pyrolysis gases, which are brought to thermodynamic equilibrium with the other gases in the reactor. Therefore, only the elemental composition (C, H, O) of the feedstock is required to model this step. The mass of char produced is given by the yield $Y_{char}$, defined according to the pyrolysis conditions in the reactor. As aggregated in

[33], the pyrolysis of beech wood particles occuring between 900 and 1400 °C may produce between 2%$_{wt}$ and 6%$_{wt}$ of char, and a pyrolysis occuring at lower temperatures can produce more than 10%$_{wt}$ of char.

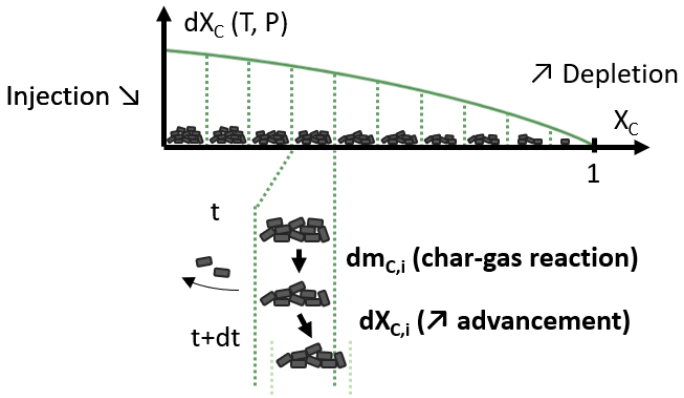


**Figure 4. Principle of char particles dynamic classification according to their conversion**

During operation, the char particles circulating in the cavity are dynamically classified according to their respective conversion. This is necessary to model oxidation reactions using RPM, as already explained in 2.3. To that extent, the particles conversion range (from 0 to 1) is segmented into ten classes of equal length (Figure 4). When a new mass of char is injected, it is added to the first class (conversion 0-0.1). Then, at each time step, the masses of the ten classes $m_{C,i}$ are updated because of heterogeneous oxidation reactions. Ten distinct conversion rates $dX_{C,i}$ are calculated, corresponding to ten mass losses $dm_{C,i}$. These masses are subtracted from the respective $m_{C,i}$, and the char populations are partly displaced towards higher conversions according to the $dX_{C,i}$ values. Finally, when particles reach the last class (conversion 0.9-1), they are integrally converted by $H_2O$, $CO_2$ and $O_2$. A sensitivity analysis showed that increasing the number of classes did not improve the results significantly.

# 3. VALIDATION OF THE SIMULATION CODE

## 3.1. Validation of the thermal model

Two thermal validation cases to compare the reactor thermal response with experimental data were proposed. The temperature responses of the reactor to several solar power steps were determined, in both direct and indirect heating modes, to adjust the thermal model parameters under argon heating. Two parameters were fitted, including the optical efficiency $\eta_{opt,receiver}$ (Equation 7) and the apparent area of the cap $A_{app}$ radiating towards the outside (Equation 12).

### 3.1.1. Direct heating mode

Under direct heating, four consecutive solar power steps were performed ($Q_{sun,1}$ equalled successively 330, 610, 950, and 1035 W), and the corresponding $T_{probe}$ and $T_{pyro}$ responses were plotted (Figure 5, $T_{probe}$ and $T_{pyro}$ lowest observable values are 200 °C and 500 °C, respectively). The pyrometer pointed towards the conical region, showing temperatures 100 °C lower than the thermocouple measurement during reactor heating. Actually, $T_{pyro}$ raw measurements did not consider any surface texture, slope and emissivity, so they might be slightly under-estimated. In comparison, the probe provided a representative measurement of $T_{wall}$, due to irradiation by the walls during operation.

A good agreement was achieved between the simulation temperature $T_{wall}$ (sim) and the probe measurement $T_{probe}$ (exp), during the reactor heating and cooling. Increasing the $\eta_{opt,receiver}$ parameter tended to increase all the temperatures because of a higher solar power input, while increasing the

$A_{app}$ value tended to decrease the highest temperatures only because of higher radiative losses. $\eta_{opt,receiver}$ was eventually fixed to 0.65, and $A_{app}$ to 7.0 cm², accounting for 13% of the total alumina cap upper area. The difference between $T_{wall}$ and $T_{gas}$ in the simulation reached up to 70 °C at high solar power input, because of the low residence time of argon in the cavity (~1 second).

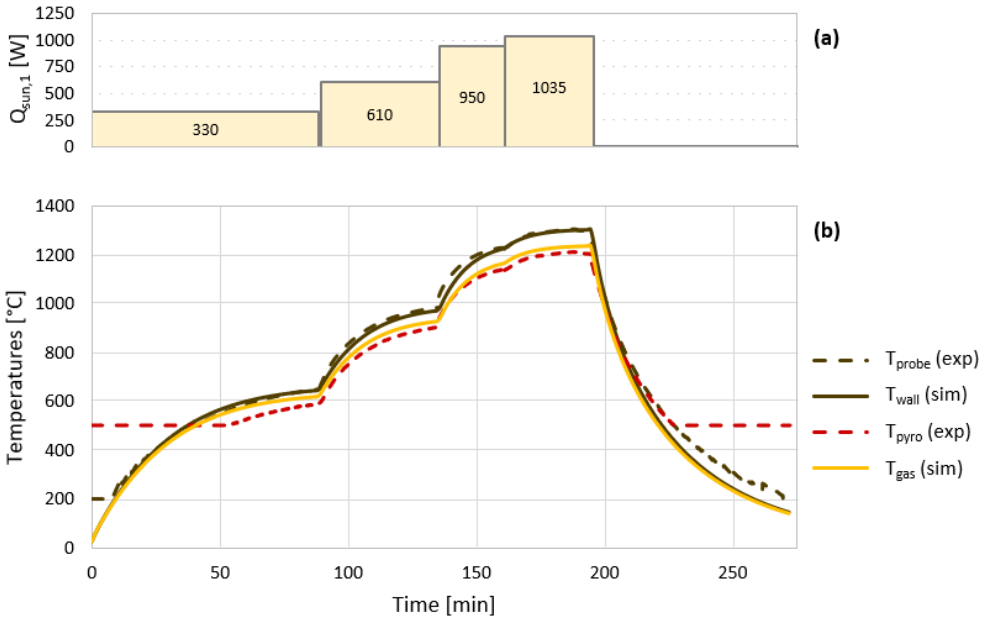


**Figure 5. (a) Solar power inputs, (b) Comparison of simulation (sim) and experimental (exp) thermal responses under argon heating (direct heating)**

### 3.1.2. Indirect heating mode

Under indirect heating, three consecutive solar power steps were performed ($Q_{sun,1}$ equalled successively 375, 705, and 1025 W), and the corresponding temperatures responses were plotted (Figure 6). In this case, $T_{pyro}$ was systematically much higher than $T_{probe}$ (120 to 350 °C of difference during reactor heating), because the pyrometer pointed towards the centre of the hot emitter plate. Higher thermal losses occurred because of this hot wall placed near the reactor aperture, thus a higher solar power input was required to let $T_{probe}$ rise beyond 1200 °C (1025 W, versus 950 W in direct heating).

The satisfying agreement between experimental and simulation data, obtained while keeping the same parameters as in Figure 5, showed the robustness of the zero-dimensional thermal model. A higher gap was however noticed between $T_{wall}$ (sim) and $T_{probe}$ (exp) than in Figure 5 (it reached 120 °C at low temperatures). $T_{gas}$ (sim) was higher than $T_{wall}$ (sim) at low temperatures due to the high contribution of the emitter plate in the heating of the reactor chamber ($T_{plate}$ is much higher than $T_{wall}$ during the first 60 minutes).

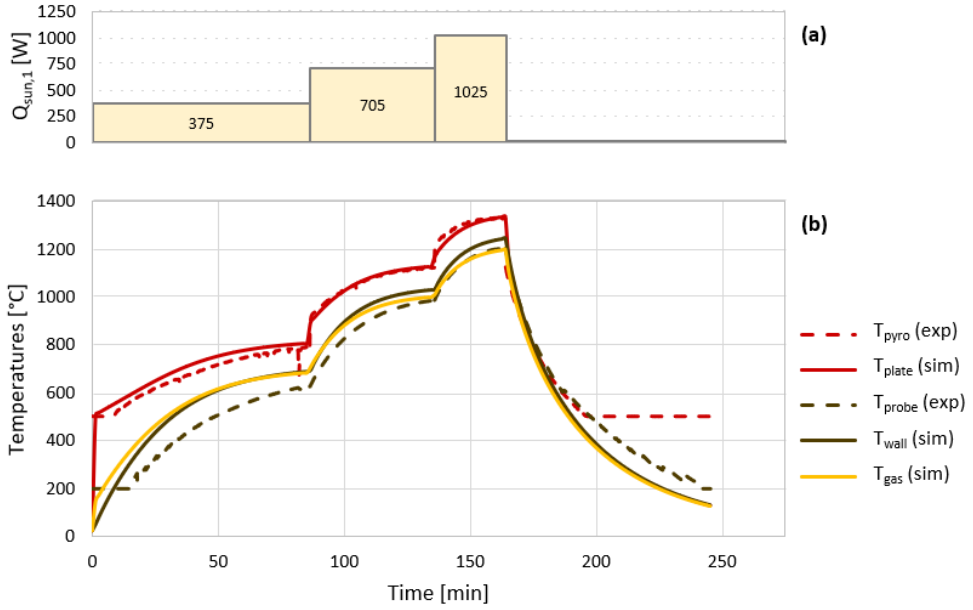


**Figure 6. (a) Solar power inputs, (b) Comparison of simulation (sim) and experimental (exp) thermal responses under argon heating (indirect heating)**

## 3.2. Validation of solar gasification dynamics

A second set of validation cases was proposed to validate the dynamics of solar gasification (Figures 7-9). The operating conditions are summed up in Table 4. Different heating modes, feedstock compositions and steam to biomass (S/B) stoichiometries were assessed. All series were carried out under a constant $T_{probe}$ temperature (1300 °C), thanks to the controlled aperture of the shutter obstructer. During the first part of the experiments (17-18 minutes), feedstock and steam were injected, producing a $H_2$ and CO-rich syngas. Then, during the second part, no feedstock was injected anymore and steam was maintained to gasify the remaining particles of char. The mass of char accumulated during the first part of the experiments was deduced by integrating the flow rates of CO, $CO_2$ and $CH_4$ produced during the second part.

**Table 4. Operating conditions for biochar and beech wood dynamic gasification runs (Figure 7 to Figure 9)**

| | Heating | Feedstock | Feedstock rate [g/min] | $H_2O$ rate [g/min] | $(S/B)/(S/B)_{st}$ |
|---|---|---|---|---|---|
| Case 1 | Indirect | Biochar | 0.23 | 0.39 | 1.13 |
| Case 2 | Indirect | Biochar | 0.23 | 0.49 | 1.42 |
| Case 3 | Direct | Beech wood | 1.2 | 0.2 | 1.13 |

### 3.2.1. Gasification of biochar

In Figure 7, the conversion of biochar was performed to validate the char gasification kinetics while minimizing the impact of devolatilization. This biochar (produced by the UK Biochar Research Centre, measured composition given in Table 5) resulted from the pyrolysis of soft-wood pellets in a 700 °C rotary kiln. The brittle centimetric cylindrical pellets were directly grinded by the screw driver before entering the cavity.

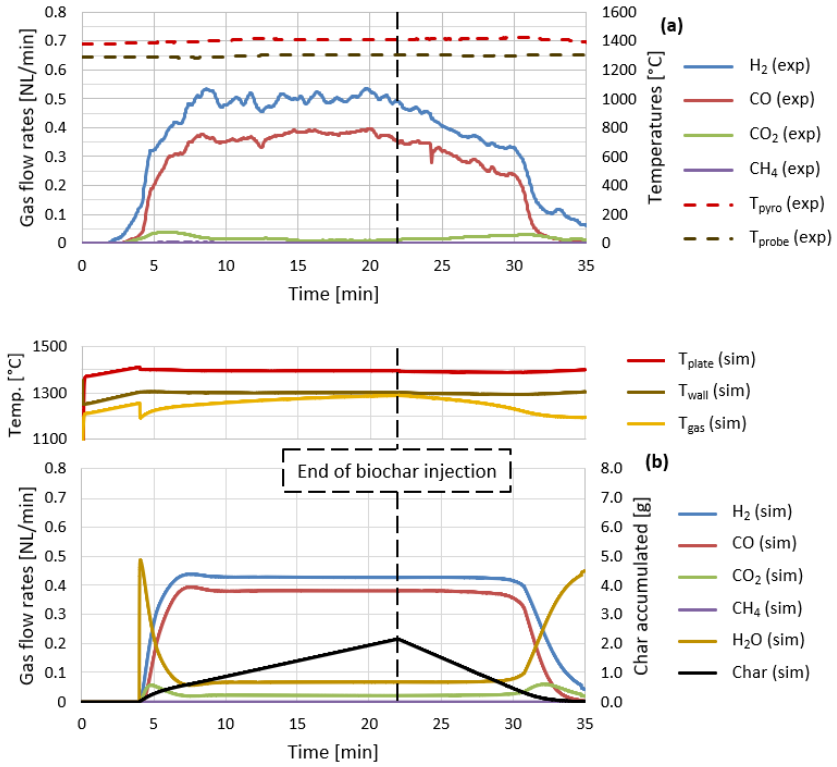


**Figure 7. (a) Experimental products outcomes and temperatures, (b) Simulation products outcomes and temperatures, during the gasification of biochar (indirect heating). $F_{biochar}$ = 0.23 g/min, $F_{steam}$ = 0.39 g/min, $T_{probe}$ = 1300 °C**

The experiments showed that $T_{probe}$ and $T_{pyro}$ temperatures were successfully maintained at 1300 and 1400 °C, respectively. Under such conditions, the production of $H_2$ and CO started plateauing around time = 10 min (reaching around 0.50 and 0.38 NL/min, respectively). A $H_2$:CO molar ratio of 1.32 was reached, resulting from the WGS reaction. Meanwhile, the $CO_2$ production stabilized around 0.01 NL/min, after peaking to 0.04 NL/min during the initial transient period. After the interruption of biochar injection, the $H_2$ and CO production rates decreased by one third between time = 22 and 30 min, and finally dropped as char consumption was nearly complete. The CO flow rate became neglectable around time = 34 min, and 10 more minutes were required to reach the end of $H_2$ production. During this transient, the $CO_2$ production peaked at 0.03 NL/min (time = 31 min) because of the higher fraction of $H_2O$ available for WGS.

Regarding simulation results, the wall temperature stabilized well at 1300 °C. $T_{plate}$ stabilized at 1400 °C, in accordance with experimental results. $T_{gas}$ increased strongly during the first 15 minutes of gasification and stabilized around 1300 °C. It then decreased until 1200 °C when biochar injection was stopped, as the solar power input was decreased to maintain $T_{wall}$ equal to 1300 °C. Compared with experimental data, the $H_2$ and CO flow rates stabilized somewhat more quickly (after 5 minutes). The $H_2$:CO molar ratio equalled only 1.12, which is the value given by gas-phase thermodynamic equilibrium. The accumulation of char in the cavity (black curve) increased until 2.16 g, and then decreased gradually after the char injection stopped. This mass was well validated by the experiment, as a 1.9 g accumulation (±0.3 g, uncertainty regarding the final carbon mass balance) was determined experimentally using a mass balance on carbon (gas phase) after biomass injection. Besides, the time necessary to gasify the char residue was similar in the experimental and simulation curves, which validated the kinetics implemented.

**Table 5. Composition of biochar pellets feedstock (dry basis)**

| Moisture [wt%] | C (dry) [wt%] | H (dry) [wt%] | O (dry) [wt%] | Ash (dry) [wt%] |
|---|---|---|---|---|

| | | | | |
|---|---|---|---|---|
| 1.0 | 90.2 | 1.8 | 6.0 | 1.9 |

Figure 8 shows the effect of a higher steam flow-rate on syngas production rates. During steady state, the experiment showed a higher $H_2$:CO molar ratio (1.38) because of the enhanced WGS reaction, and a higher $CO_2$ production rate (0.03 NL/min) than in Figure 7. The simulation showed that only 1.32 g of char was accumulated in the cavity, while a 1.0 g accumulation (±0.1 g) was determined experimentally. Less time was therefore required to gasify the residue during the second part of the experiment than in Figure 7. Once again, a satisfying agreement was found between experimental and simulation data, and the impact of steam stoichiometry was well represented by the model.

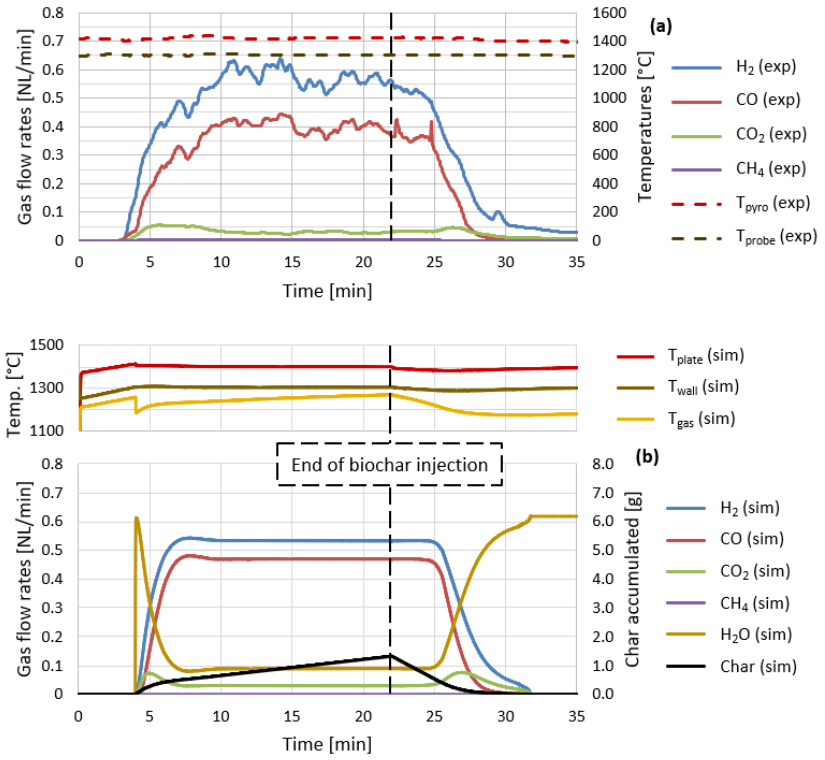


**Figure 8. (a) Experimental products outcomes and temperatures, (b) Simulation products outcomes and temperatures, during the gasification of biochar (indirect heating). $F_{biochar}$ = 0.23 g/min, $F_{steam}$ = 0.49 g/min, $T_{probe}$ = 1300 °C**

### 3.2.2. Gasification of beech wood

The pyro-gasification of beech wood was then performed (Figure 9). This new validation case enabled validating the devolatilization mechanism implemented in DEMOSTRAR. Three different char yields (8%$_{wt}$, 12%$_{wt}$ and 16%$_{wt}$) were assessed in the simulation results, corresponding to decreasing pyrolysis temperature conditions (see Section 2.6). Different pyrolysis temperatures could indeed be encountered, caused by the feedstock progressive heating in the screw driver.

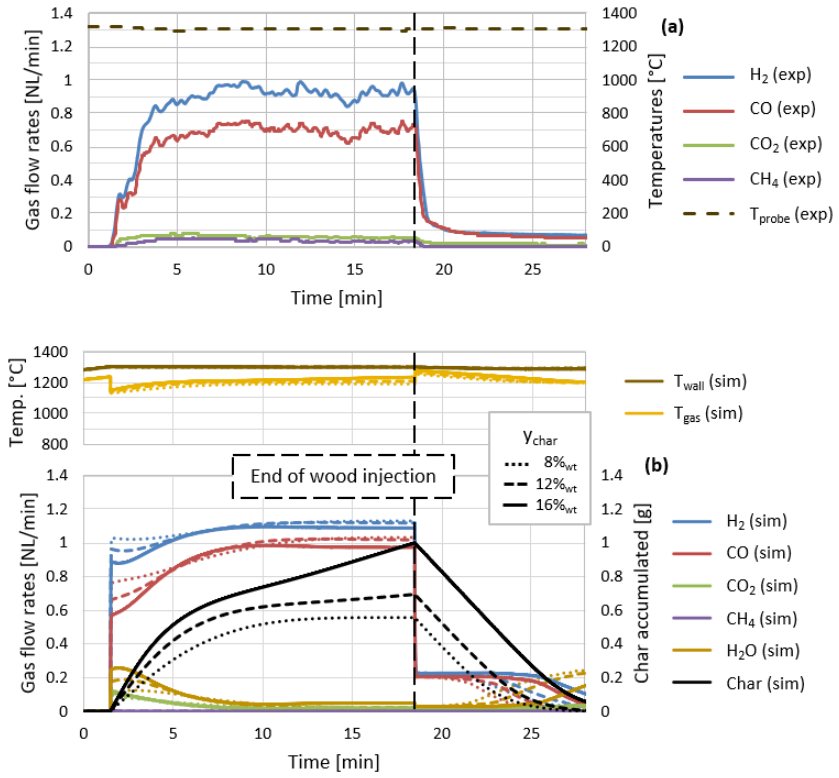


**Figure 9. (a) Experimental products outcomes and temperatures, (b) Simulation products outcomes and temperatures, during the gasification of beech wood (direct heating). $F_{wood}$ = 1.2 g/min, $F_{steam}$ = 0.2 g/min, $T_{probe}$ = 1300 °C**

Experimental data showed the establishment of a stable syngas production regime after ~5 minutes of injection (~0.95 NL/min $H_2$ and 0.70 NL/min CO). When wood injection stopped, a prompt decrease of syngas production was observed as no pyrolysis took place anymore. The remaining char was gasified slowly, over more than 20 minutes. In comparison, simulation results showed the establishment of higher production rates of $H_2$ and CO (~1.1 and 1.0 NL/min, respectively) and lower production rates of $CO_2$ and $CH_4$. This was mainly due to the thermodynamic equilibrium hypothesis.

According to the simulation, the chemical and thermal transients were strongly affected by the yield of char. Higher yields caused increasing char accumulations, and favoured the heating of the reactor content due to higher particles radiative absorptivity. At equilibrium, $T_{gas}$ equalled 1191, 1210 and 1234 °C at $Y_{char}$ = 8%$_{wt}$, 12%$_{wt}$ and 16%$_{wt}$, respectively. Besides, higher yields led to a steeper progression of $H_2$ and CO production rates. When the wood injection was stopped, the accumulation of char equalled 0.56, 0.69 and 1.00 g at $Y_{char}$ = 8%$_{wt}$, 12%$_{wt}$ and 16%$_{wt}$, respectively. In comparison, the accumulation determined experimentally was 0.71 g (±0.08 g).

This comparison highlighted the role of the screw driver, that led to pyrolysis starting at temperatures lower than $T_{gas}$. In the following, $Y_{char}$ will be set to 12%$_{wt}$, that is the value better validated by experimental data for this reactor design.

## 3.3. Validation of hybridized gasification results

A validation of the model was performed with beech wood pyro-gasification experimental results, in the case of hybridization with *in-situ* oxygen injection [29]. The aim was to control the syngas quality ($H_2$:CO ratio) during hybridization by conjointly increasing the steam injection rate. The results were obtained under direct solar heating, with $T_{probe}$ being constantly maintained at 1300 °C. The flow rates of reactants and the comparison between experimental (exp) and simulation (sim) results are provided in the bar charts of Figure 10.

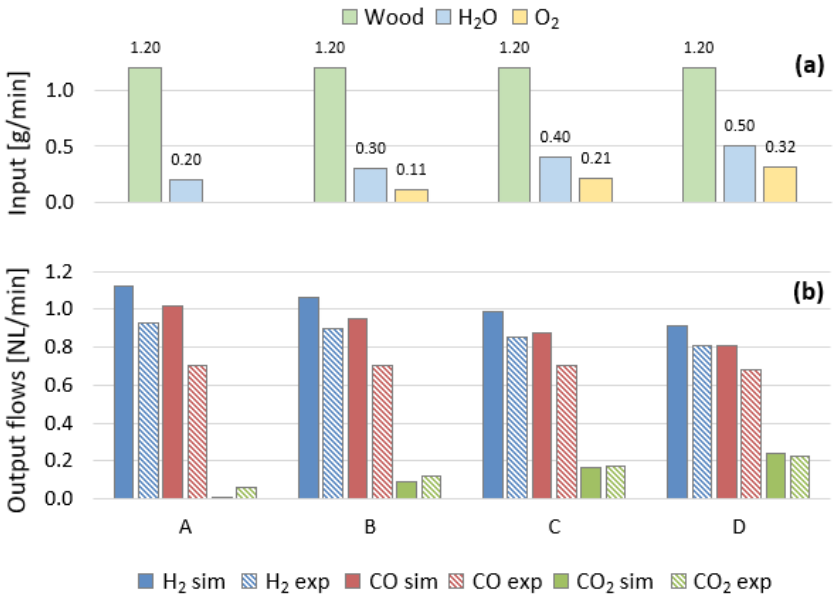


**Figure 10. (a) Input flow rates, (b) Comparison of simulation (sim) and experimental (exp) syngas compositions, during the hybridized gasification of beech wood (direct heating, $T_{probe}$ = 1300 °C)**

Figure 10 shows a fair agreement between experimental and simulation data. The relative discrepancy regarding $H_2$, CO and $CO_2$ production rates was lower than 31%, with the exception of $CO_2$ production during run A. Both the $H_2$ and CO productions decreased at a comparable rate during hybridization, while the production of $CO_2$ increased progressively because of combustion reactions. The $H_2$:CO molar ratio was maintained near its initial value thanks to the injection of steam, according to both the simulation data (slightly increasing from 1.10 to 1.13) and the experimental data (slightly decreasing from 1.32 to 1.19). Actually, it would have decreased drastically if no steam had been supplied [29]. The coupled impact of oxygen and steam injection rates was thus well represented by the DEMOSTRAR model, despite an over-estimation of $H_2$ and CO flow rates due to mainly the thermodynamic equilibrium hypothesis and to the imprecise wood injection rates over long experiments [29].

# 4. PARAMETRIC ANALYSIS

After the validation step, the model was employed to assess the impact of reactants flow rates on reactor temperatures, char accumulation, chemical species outputs and efficiencies.

## 4.1. Impact of steam input flow rate

The impact of steam injection rate on the reactor products outcome was investigated. Figure 11 illustrates the char accumulation dynamics under several steam flow rates. The input solar power was maintained constant ($Q_{sun,1}$ = 1200 W, direct heating), as the gasification of 1.2 g/min of beech wood was simulated. At this feeding rate, a $H_2O$ flow-rate of 0.165 g/min was theoretically required to achieve stoichiometry. Two kinds of responses were actually observed:

- At $F_{H2O} \leq 0.2$ g/min, the quantity of char accumulated in the cavity diverged over time.
- At $F_{H2O} \geq 0.3$ g/min, the quantity of char accumulated converged after 30 minutes.

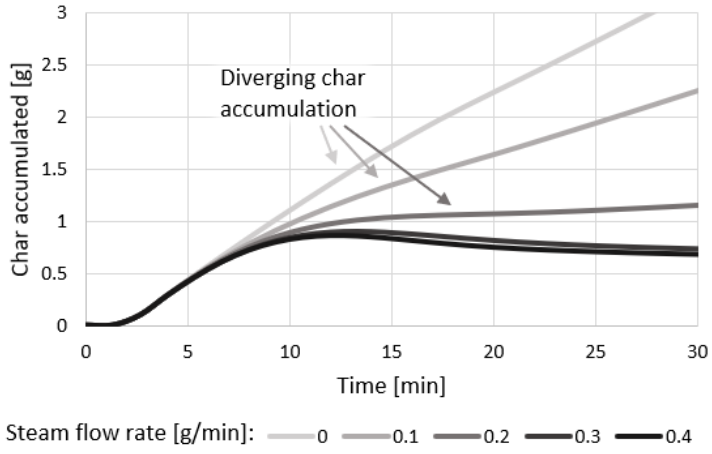


**Figure 11. Char accumulation dynamics, for different steam injection rates (0-0.4 g/min). $F_{wood}$ = 1.2 g/min, $Q_{sun,1}$ = 1200 W**

Figure 12 illustrates more in details the impact of steam injection rate on the reactor temperatures, the accumulation of char, and the reactor chemical performances. Simulations were performed with a wood feeding rate of 1.2 g/min, and solar power inputs $Q_{sun,1}$ ranging from 975 to 1425 W. The maximal steam injection rate was 0.6 g/min. All the simulated data provided here were collected when steady state was reached, regarding both the temperatures and the accumulation of char. The minimal steam flow rate ensuring char mass convergence was ~0.22 g/min, that was 1.33 times the theoretical steam-gasification stoichiometry (0.165 g/min), because of kinetic limitations and short steam residence times.

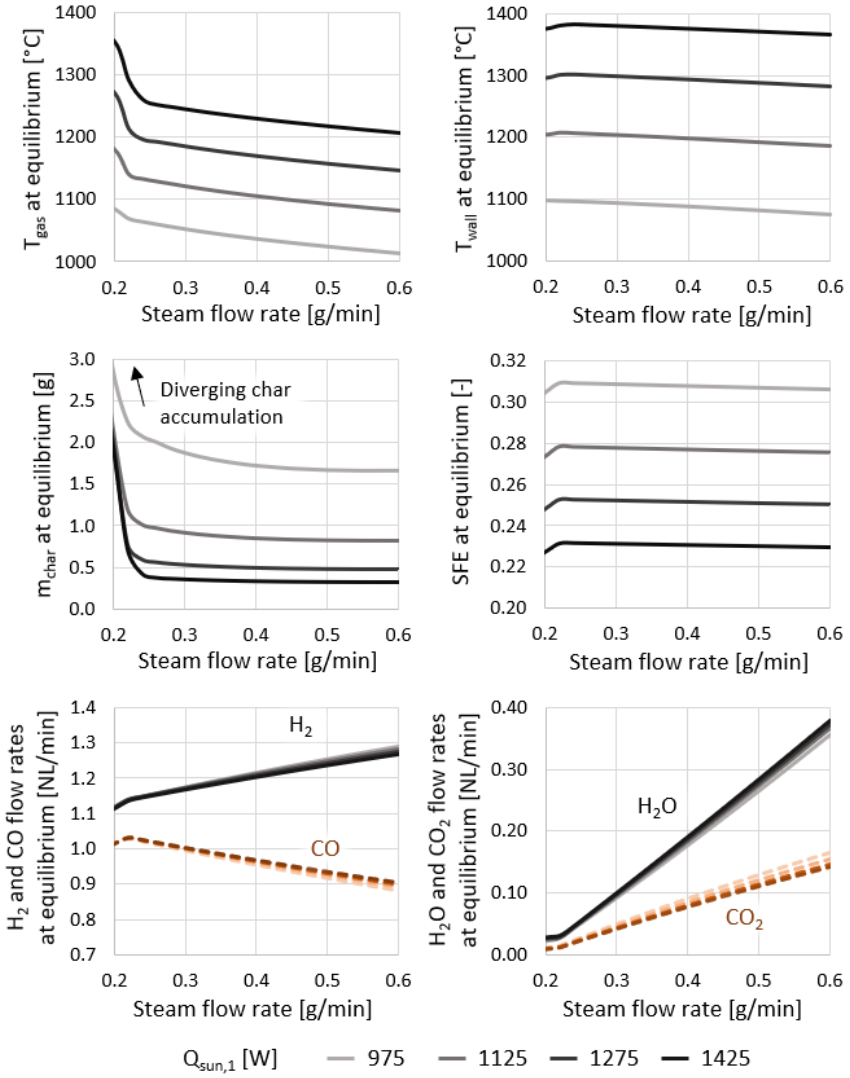


**Figure 12. Impact of steam flow rate on reactor temperatures, char accumulation, SFE and chemical outcome, for different solar power inputs ($Q_{sun,1}$, 975-1425 W). $F_{wood}$ = 1.2 g/min**

Increasing the steam input above 0.22 g/min resulted in $T_{gas}$ decreasing by ~100 °C, and $T_{wall}$ decreasing by ~25 °C because of higher heating requirements. Char accumulation decreased, especially at the lowest solar power inputs (from 2.1 to 1.7 g), due to favoured steam-gasification kinetics. The production of $H_2$+CO remained constant (2.17 NL/min), while the molar $H_2$:CO ratio increased strongly because of enhanced WGS (from 1.13 to 1.47 at the lowest $Q_{sun,1}$), as observed in [29]. The Solar-to-Fuel Efficiency (SFE, Equation 14) decreased very slightly, as the molar LHV of $H_2$ (240.2 kJ/mol) is lower than the molar LHV of CO (282.8 kJ/mol). Meanwhile, the $H_2O$ and $CO_2$ outputs increased linearly.

$$\mathrm{SFE} = \frac{\mathrm{LHV}_{\mathrm{H_2}} \cdot \dot{m}_{\mathrm{H_2}} + \mathrm{LHV}_{\mathrm{CO}} \cdot \dot{m}_{\mathrm{CO}} + \mathrm{LHV}_{\mathrm{CH_4}} \cdot \dot{m}_{\mathrm{CH_4}}}{\mathrm{Q}_{\mathrm{sun,1}} + \mathrm{LHV}_{\mathrm{wood}} \cdot \dot{m}_{\mathrm{wood}}} \quad (14)$$

Increasing the solar power input naturally led to higher temperatures, and lower char accumulation and SFE. High solar power inputs caused the reactor walls temperature to approach 1400 °C, which would degrade the FeCrAl alloy constituting the reactor wall. Contrarily, low solar power inputs substantially increased the SFE, while decreasing $T_{gas}$ and increasing the accumulation of char.

## 4.2. Impact of biomass input flow rate

The impact of wood feeding rate (1 to 3 g/min) on the reactor temperatures, char accumulation and SFE was studied (Figure 13), under solar power inputs in the range 975-1425 W. The mass ratio between steam and injected wood (wet) was maintained equal to 0.25.

Because of the endothermal reaction, both the gas and wall temperatures decreased, as wood was injected, by 200 to 250 °C. Converting more wood yielded a higher syngas output. The SFE thus increased from 0.22 to 0.47, following the path where $Q_{sun,1}$ = 1275 W/m². Finally, the gasification of more wood led to higher char accumulation in the reactor, that could go beyond 5 g at the lowest $Q_{sun,1}$. The mass of char eventually diverged over time, when too much wood was provided at a given $Q_{sun,1}$, so the curves of Figure 13 had to be interrupted whenever steady state could not be reached.

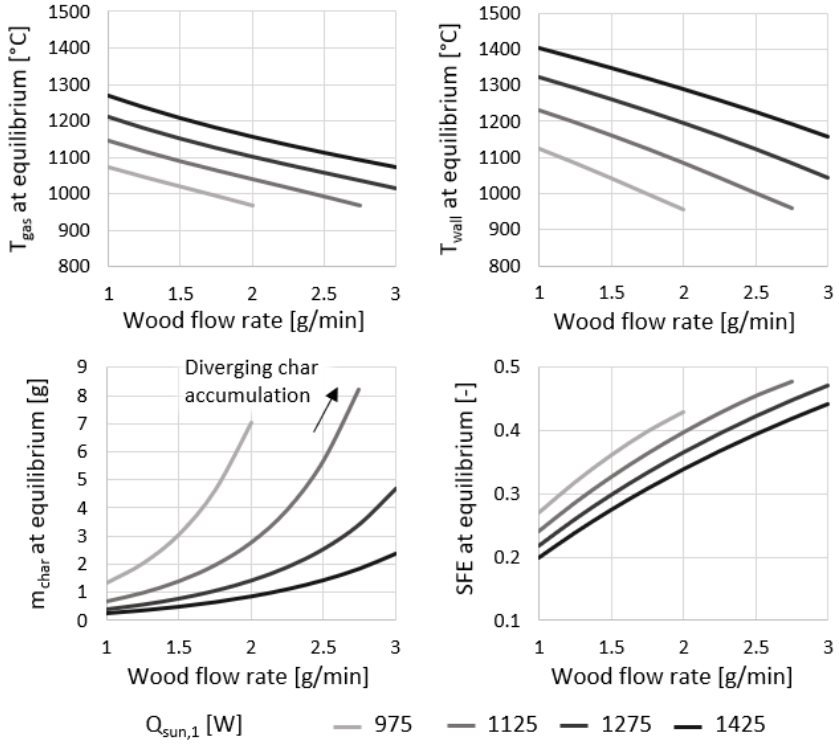


**Figure 13. Impact of wood flow rate on reactor temperatures, char accumulation and SFE, for different solar power inputs ($Q_{sun,1}$, 975-1425 W). Steam/wood$_{(wet)}$ = 0.25 g/g**

Once again, increasing the solar power input increased the reactor temperatures, and thus decreased the accumulation of char. Maintaining the wall temperature at 1300 °C while injecting more than 2.0 g/min of biomass would require to increase $Q_{sun,1}$ above 1425 W, which is prevented due to solar concentrator limitations.

## 4.3. Impact of oxygen input flow rate

The impact of oxygen addition in the reactor was finally assessed. The initial case was the allothermal steam gasification of 1.2 g/min of wood, under a solar power input $Q_{sun,1}$ of 1125 W. From this point, injecting oxygen alone would have caused temperatures to reach dramatically high values. Instead, the addition of oxygen was associated with a proportional decrease of the solar power input.

### 4.3.1. Hybridization at constant wood flow rate

In Figure 14, the oxygen flow rate was raised from 0 to 1.1 NL/min (Equivalence Ratio defined in Equation 15, ER = 0.97), while $Q_{sun,1}$ was decreased from 1125 to 0 W (-102.3 W per 0.1 NL/min of $O_2$ provided). The wood flow rate was maintained constant. These specific conditions enable to range from the solar gasification of biomass to its integral combustion, while maintaining a relatively stable

$T_{gas}$ temperature. In a first domain ($F_{O2}$ < 0.6 NL/min), char accumulation was reduced because of combustion until 30 mg. The gas temperature decreased down to 1000°C, as oxy-combustion did not counteract the decreasing solar power input. In a second domain ($F_{O2}$ > 0.6 NL/min), $T_{gas}$ increased, reaching up to 1042 °C during autothermal operation. Besides, during the entire hybridization path, the wall temperature decreased despite combustion occurring in the cavity. It went below $T_{gas}$ around $F_{O2}$ = 0.65 NL/min, and reached down to 854 °C during autothermal operation. Both the $H_2$ and CO production rates decreased strongly because of oxy-combustion, with a declining $H_2$:CO molar ratio, until they reached zero at $F_{O2}$ = 1.1 NL/min. Increasing amounts of $CO_2$ and $H_2O$ were produced due to combustion reactions. As a result, the Cold-Gas Efficiency (CGE, Equation 16) decreased linearly with the oxygen input (-0.10 per 0.1 NL/min of $O_2$ provided), in agreement with experimental results [28] (proportional relation between the $O_2$:C ratio increase and the CGE decrease). A CGE higher than 1 (1.12 in allothermal gasification) indicated that the fuel heat content was upgraded, storing a part of the incident solar energy. A CGE lower than 1 indicated that a downgrade occurred, especially because gases with high LHV were combusted.

$$\mathrm{ER} = (\mathrm{n_{biomass}}/\mathrm{n_{O2}})/(\mathrm{n_{biomass}}/\mathrm{n_{O2}})_{\text{combustion stoichiometry}} \quad (15)$$

$$\mathrm{CGE} = \frac{\mathrm{LHV_{H_2}} \cdot \dot{\mathrm{m}}_{\mathrm{H_2}} + \mathrm{LHV_{CO}} \cdot \dot{\mathrm{m}}_{\mathrm{CO}} + \mathrm{LHV_{CH_4}} \cdot \dot{\mathrm{m}}_{\mathrm{CH_4}}}{\mathrm{LHV_{wood}} \cdot \dot{\mathrm{m}}_{\mathrm{wood}}} \quad (16)$$

Increasing the steam injection rate from 0.3 to 0.6 g/min did not significantly affect the CGE. It decreased $T_{gas}$ by 39 to 55 °C (allothermal and autothermal operation, respectively), and $T_{wall}$ by 17 to 32 °C (allothermal and autothermal operation, respectively). It also decreased the mass of char accumulated, only under allothermal operation. Obviously, increasing the injection of steam resulted in much higher $H_2O$ outputs, and also higher $CO_2$ outputs near allothermal operation because of the WGS reaction.

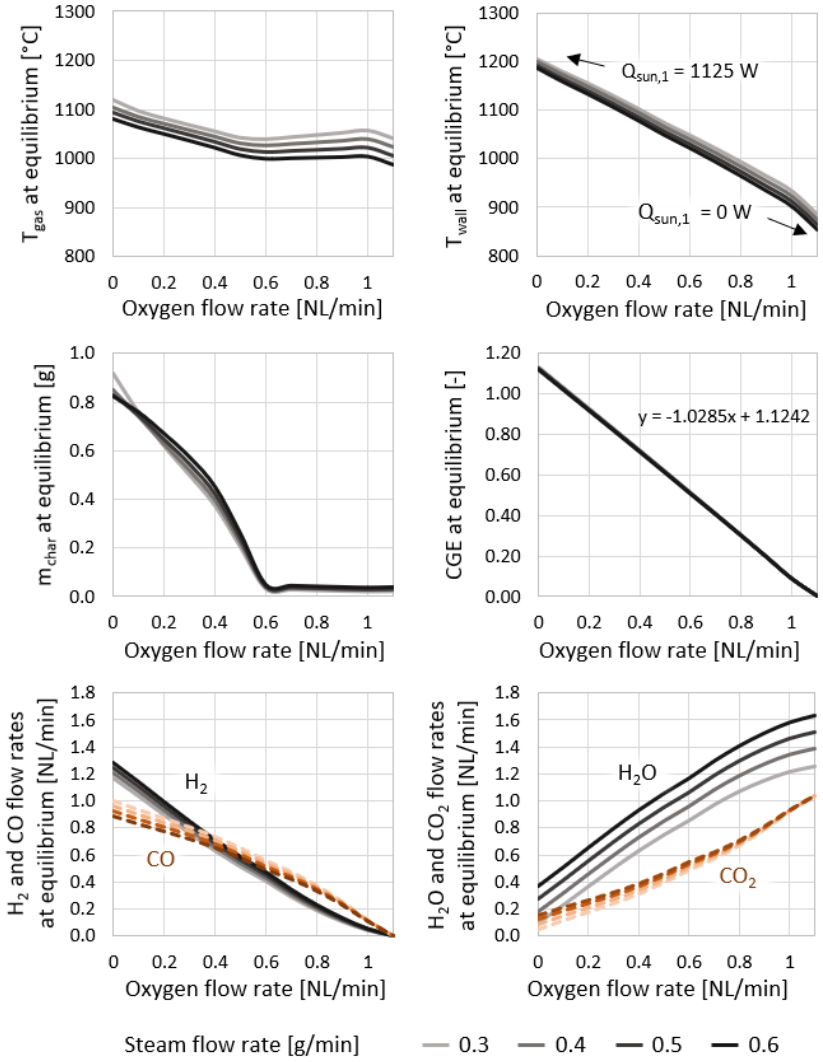


**Figure 14. Impact of oxygen flow rate on reactor temperatures, char accumulation, CGE and chemical outcome, for different steam inputs (0.3-0.6 g/min) under decreasing solar power input ($Q_{sun,1}$, 1125-0 W). $F_{wood}$ = 1.2 g/min**

### 4.3.2. Hybridization at increasing wood flow rate

A similar parametric study was performed in Figure 15, but the decrease of $H_2$ and CO was compensated by a gradual addition of biomass during hybridization. The wood flow rate was increased from 1.2 to 3.2 g/min, while the oxygen flow rate was increased from 0 to 1.8 NL/min (ER = 1.58). The solar power $Q_{sun,1}$ kept on decreasing gradually from 1125 to 0 W. In this case, the gas temperature remained between 1045 and 1120 °C, while $T_{wall}$ decreased down to 920 °C. The $H_2$+CO volume flow rate was successfully maintained constant (2.17 NL/min) despite hybridization, at the cost of a much higher production of $H_2O$ and $CO_2$. In this case, the CGE decreased less than in Figure 14, as its minimal value (autothermal operation) reached 0.44.

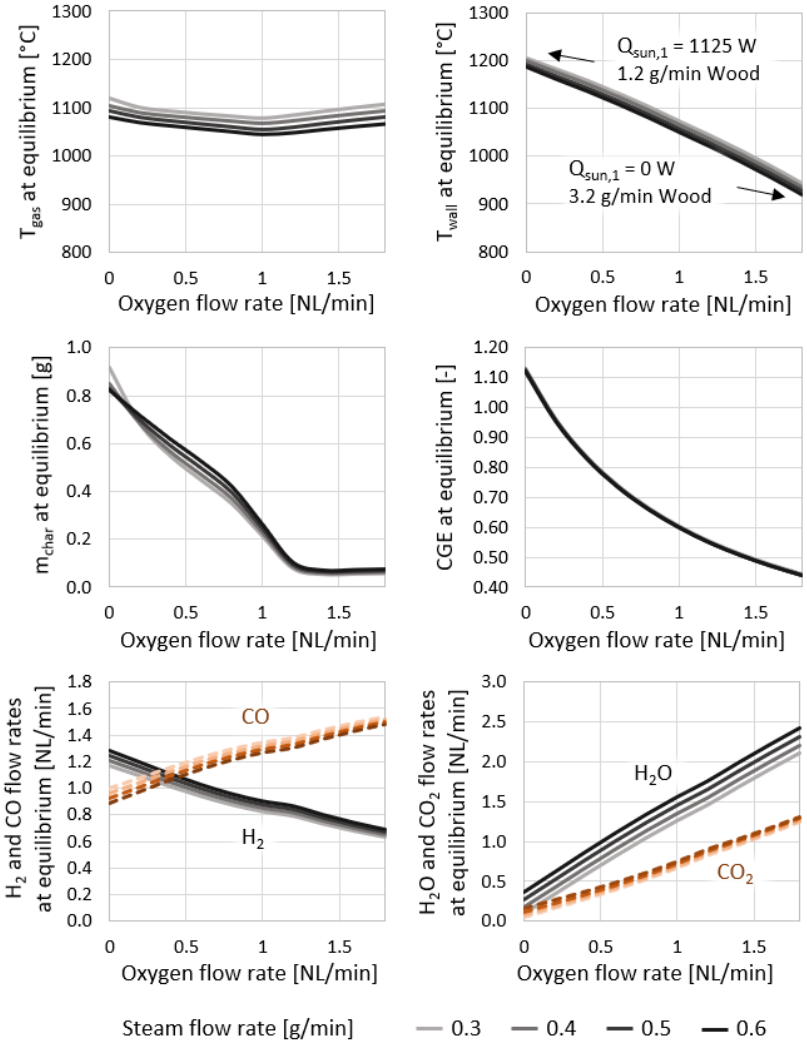


**Figure 15. Impact of oxygen flow rate on reactor temperatures, char accumulation, CGE and chemical outcome, for different steam inputs (0.3-0.6 g/min), under decreasing solar power input ($Q_{sun,1}$, 1125-0 W) and increasing wood input (1.2-3.2 g/min)**

Thermal and mass balances were proposed in Figure 16, corresponding to the hybridization studied in Figure 15 with $F_{H2O}$ = 0.4 g/min. Four oxygen flow rates from 0 to 1.8 NL/min were assessed, with decreasing solar power inputs and increasing wood feeding rates. In Figure 16-a, the sum of the solar power input $Q_{sun,2}$ and the heat delivered by combustion was provided. Against it, the sum of the useful heat, as well as the radiative (rad) and conductive (cnd) heat losses was plotted. The total heat required to operate the reactor decreased through hybridization, because of the decreasing heat losses occurring at the wall. The reactor efficiency (useful heat over total heat source) thus increased from 0.29 to 0.40. Regarding the mass balances (Figure 16-b), the increase of $O_2$ and wood flow rates caused an increase of all the output flow rates excepting hydrogen. The $CH_4$ output was negligible, as well as the $C_2H_2$ output, whatever the heating modes and operating conditions.

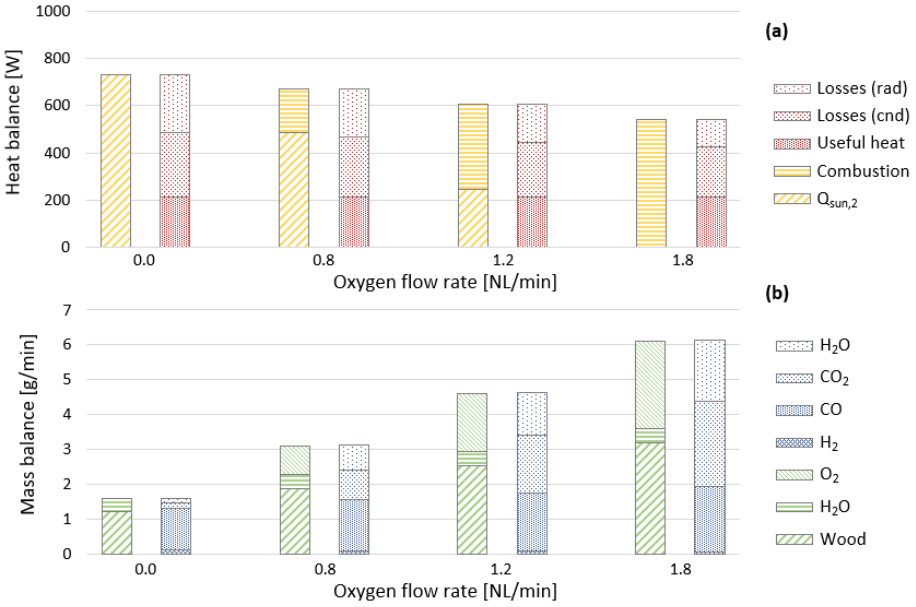


**Figure 16. (a) Heat and (b) Mass balances, following the hybridization path of Figure 15. $F_{H2O}$ = 0.4 g/min**

# 5. CONCLUSIONS

A dynamic simulation code was developed to model a solar-autothermal hybrid gasifier. This code assumed that the gas phase was at thermodynamic equilibrium, while the oxidation of solid char particles was ruled by detailed heterogeneous kinetics to describe the accumulation of char during transients. This improvement enabled to unravel key dynamic phenomena regarding woody biomass gasification, at a limited calculation cost (1 minute required to simulate 100 minutes of operation, with a time step of 0.2 seconds). Simulations reliably predicted the reactor thermal response up to 1300 °C under both direct and indirect solar heating, and syngas production rates under both solar and solar-autothermal hybridized operations.

- The thermal validation against experimental data was successful, showing wall temperature discrepancies below 50 °C under direct heating and 120 °C under indirect heating (the maximal temperature assessed being 1300 °C).
- The validation of solar-autothermal hybrid gasification was satisfying, with a syngas flow rate discrepancy explained by the gas-phase thermodynamic equilibrium assumption.
- Char accumulation usually converged after 30 minutes, when the steam input was higher than 1.33 times the theoretical stoichiometry, due to kinetic limitations in the reactor.
- Providing excess steam (0.22-0.60 g/min) resulted in improved $H_2$:CO molar ratios (1.13-1.47 at $Q_{sun,1}$ = 975 W), and did not decrease the $H_2$+CO production.
- Increasing the wood feeding rate (1-3 g/min) doubled the SFE (0.22-0.47 at $Q_{sun,1}$ = 1275 W), but altered the reactor temperatures and caused booming char accumulation.
- Switching between solar and autothermal operation was possible, whether by keeping the wood feeding rate constant (equivalence ratio reaching 0.97, *i.e.,* total combustion of feedstock) or by increasing it to maintain a constant production of $H_2$+CO (equivalence ratio reaching 1.58).

The DEMOSTRAR model is therefore suitable for an application to reactor optimization and dynamic control. Accordingly, it will be specifically applied to the control of syngas production output based on various control variables and optimization schemes to identify suitable strategies for process hybridization. The main optimization goals will be to minimize the consumption of both oxygen and solid feedstock as well as the $CO_2$ emissions, while achieving maximum or stable syngas ($H_2$+CO)

production under variable (daily fluctuations) and intermittent solar energy input for 24/7 continuous operation. Further work will address the implementation of alternative hybridization pathways, considering e.g., concentrated solar resource combined with external combustion, electrical heating or thermal energy storage. Annual performance and environmental impact assessments of solar gasification plants will finally be performed.

# NOMENCLATURE

**Abbreviations**

- CGE Cold-Gas Efficiency
- DEMOSTRAR Dynamic, Extrapolation-ready Modelling and Optimization of a Solar Thermochemical ReActoR
- DNI Direct Normal Irradiance (W/m²)
- RPM Random-Pore Model
- SFE Solar-to-Fuel Efficiency
- WGS Water-Gas Shift

**Physical variables**

| | | |
|---|---|---|
| • $\alpha_{char}$ | [-] | Volumetric absorptivity of light by char particles |
| • $\alpha_{gas}$ | [-] | Volumetric absorptivity of light by gases ($H_2O$, $CO_2$) |
| • $\varepsilon_{gas}$ | [-] | Volumetric emissivity of light by gases ($H_2O$, $CO_2$) |
| • $\delta_{shutter}$ | [-] | Fraction of aperture of the shutter obstructer |
| • $\psi$ | [-] | Structure parameter, used in RPM |
| • $\eta_{opt,concentrator}$ | [-] | Optical efficiency of the heliostat + concentrator facility |
| • $\eta_{opt,receiver}$ | [-] | Optical efficiency of the window + zirconia felts restriction |
| • $A_{proj}$ | [m²] | Parabolic concentrator area irradiated by sunlight (horizontal projection, considering the reactor shading effect) |
| • $C_X$ | [kmol/m³] | Molar concentration of the gas component X |
| • $F_X$ | [kg/s – NL/s] | Flow rate of species X |
| • $m_C$ | [kg] | Mass of carbon |
| • $P_X$ | [Pa] | Partial pressure of the gas component X |
| • $Q_{loss,X}$ | [W] | Heat flux lost by the reactor |
| • $Q_{sun,1}$ | [W] | Solar power delivered by the parabolic concentrator |
| • $Q_{sun,2}$ | [W] | Solar power available at the cavity entrance |
| • $Q_{X-Y}$ | [W] | Heat flux between two system components X and Y |
| • $T_{probe}$ | [K] | Temperature measurement by the thermocouple |
| • $T_{pyro}$ | [K] | Temperature measurement by the pyrometer |
| • $T_{gas}$ | [K] | Temperature of the gas + char phase in simulations |
| • $T_{wall}$ | [K] | Temperature of the wall (inner layer) in simulations |
| • $X_C$ | [-] | Advancement of a carbon mass oxidation |
| • $Y_{char}$ | [-] | Char mass yield obtained after devolatilization (dry basis) |

# DECLARATION OF COMPETING INTEREST

The authors declare that they have no known competing financial interests or personal relationships that could have appeared to influence the work reported in this paper.

## ACKNOWLEDGEMENTS

This work received partial funding from the European Union's Horizon 2020 research and innovation programme under grant agreement No 823802 (project SFERA-III), along with financial support from CEA (French Alternative Energy and Atomic Energy Commission) and Région Occitanie for the PhD grant of A. Curcio. The authors thank the UK Biochar Research Center for biochar sample supply.

## REFERENCES

[1] D.W. Gregg, R.W. Taylor, J.H. Campbell, Solar gasification of coal, activated carbon, coke and biomass mixtures, (1980) 12.

[2] R.W. Taylor, R. Berjoan, J.P. Coutures, Solar gasification of carbonaceous materials, Solar Energy. 30 (1983) 513–525. https://doi.org/10.1016/0038-092X(83)90063-4.

[3] McKendry - 2002 - Energy production from biomass (part 3) gasificat.pdf, (n.d.).

[4] M. Puig-Arnavat, E.A. Tora, J.C. Bruno, A. Coronas, State of the art on reactor designs for solar gasification of carbonaceous feedstock, Solar Energy. 97 (2013) 67–84. https://doi.org/10.1016/j.solener.2013.08.001.

[5] N. Piatkowski, C. Wieckert, A.W. Weimer, A. Steinfeld, Solar-driven gasification of carbonaceous feedstock - A review, Energy Environ. Sci. 4 (2011) 73–82. https://doi.org/10.1039/C0EE00312C.

[6] A. Gómez-Barea, M. Suárez-Almeida, A. Ghoniem, Analysis of fluidized bed gasification of biomass assisted by solar-heated particles, Biomass Conv. Bioref. 11 (2021) 143–158. https://doi.org/10.1007/s13399-020-00865-0.

[7] H. Cui, J.R. Grace, Spouting of biomass particles: A review, Bioresource Technology. 99 (2008) 4008–4020. https://doi.org/10.1016/j.biortech.2007.04.048.

[8] S. Abanades, S. Rodat, H. Boujjat, Solar thermochemical green fuels production: A review of biomass pyro-gasification, solar reactor concepts and modelling methods, Energies. 14 (2021) 1494. https://doi.org/10.3390/en14051494.

[9] N. Piatkowski, C. Wieckert, A. Steinfeld, Experimental investigation of a packed-bed solar reactor for the steam-gasification of carbonaceous feedstocks, Fuel Processing Technology. 90 (2009) 360–366. https://doi.org/10.1016/j.fuproc.2008.10.007.

[10] F. Müller, P. Poživil, P.J. van Eyk, A. Villarrazo, P. Haueter, C. Wieckert, G.J. Nathan, A. Steinfeld, A pressurized high-flux solar reactor for the efficient thermochemical gasification of carbonaceous feedstock, Fuel. 193 (2017) 432–443. https://doi.org/10.1016/j.fuel.2016.12.036.

[11] G.J. Nathan, B.B. Dally, Z.T. Alwahabi, P.J. van Eyk, M. Jafarian, P.J. Ashman, Research challenges in combustion and gasification arising from emerging technologies employing directly irradiated concentrating solar thermal radiation, Proceedings of the Combustion Institute. 36 (2017) 2055–2074. https://doi.org/10.1016/j.proci.2016.07.044.

[12] S. Bellan, T. Kodama, K. Matsubara, N. Gokon, H.S. Cho, K. Inoue, Thermal performance of a 30 kW fluidized bed reactor for solar gasification: A CFD-DEM study, Chemical Engineering Journal. 360 (2019) 1287–1300. https://doi.org/10.1016/j.cej.2018.10.111.

[13] H. Boujjat, S. Rodat, S. Chuayboon, S. Abanades, Numerical simulation of reactive gas-particle flow in a solar jet spouted bed reactor for continuous biomass gasification, International Journal of Heat and Mass Transfer. 144 (2019) 118572. https://doi.org/10.1016/j.ijheatmasstransfer.2019.118572.

[14] J. Petrasch, P. Osch, A. Steinfeld, Dynamics and control of solar thermochemical reactors, Chemical Engineering Journal. 145 (2009) 362–370. https://doi.org/10.1016/j.cej.2008.07.051.

[15] H. Boujjat, G.M. Yuki Junior, S. Rodat, S. Abanades, Dynamic simulation and control of solar biomass gasification for hydrogen-rich syngas production during allothermal and hybrid solar/autothermal operation, International Journal of Hydrogen Energy. 45 (2020) 25827–25837. https://doi.org/10.1016/j.ijhydene.2020.01.072.

[16] S. Rodat, S. Abanades, H. Boujjat, S. Chuayboon, On the path toward day and night continuous solar high temperature thermochemical processes: A review, Renewable and Sustainable Energy Reviews. 132 (2020) 110061. https://doi.org/10.1016/j.rser.2020.110061.
[17] W.L. Saw, P. Guo, P.J. van Eyk, G.J. Nathan, Approaches to accommodate resource variability in the modelling of solar driven gasification processes for liquid fuels synthesis, Solar Energy. 156 (2017) 101–112. https://doi.org/10.1016/j.solener.2017.05.085.
[18] M. Baratieri, P. Baggio, L. Fiori, M. Grigiante, Biomass as an energy source: Thermodynamic constraints on the performance of the conversion process, Bioresource Technology. 99 (2008) 7063–7073. https://doi.org/10.1016/j.biortech.2008.01.006.
[19] A. Ramos, E. Monteiro, A. Rouboa, Numerical approaches and comprehensive models for gasification process: A review, Renewable and Sustainable Energy Reviews. 110 (2019) 188–206. https://doi.org/10.1016/j.rser.2019.04.048.
[20] P. Baggio, M. Baratieri, L. Fiori, M. Grigiante, D. Avi, P. Tosi, Experimental and modeling analysis of a batch gasification/pyrolysis reactor, Energy Conversion and Management. 50 (2009) 1426–1435. https://doi.org/10.1016/j.enconman.2009.03.004.
[21] D. Baruah, D.C. Baruah, Modeling of biomass gasification: A review, Renewable and Sustainable Energy Reviews. 39 (2014) 806–815. https://doi.org/10.1016/j.rser.2014.07.129.
[22] Q. Bellouard, S. Abanades, S. Rodat, Biomass gasification in an innovative spouted-bed solar reactor: Experimental proof of concept and parametric study, Energy Fuels. 31 (2017) 10933–10945. https://doi.org/10.1021/acs.energyfuels.7b01839.
[23] S. Chuayboon, S. Abanades, S. Rodat, Comprehensive performance assessment of a continuous solar-driven biomass gasifier, Fuel Processing Technology. 182 (2018) 1–14. https://doi.org/10.1016/j.fuproc.2018.10.016.
[24] C.D. Blasi, Comparison of semi-global mechanisms for primary pyrolysis of lignocellulosic fuels, J. Anal. Appl. Pyrolysis. (1998) 22.
[25] A.P. Muroyama, I. Guscetti, G.L. Schieber, S. Haussener, P.G. Loutzenhiser, Design and demonstration of a prototype 1.5 kWth hybrid solar/autothermal steam gasifier, Fuel. 211 (2018) 331–340. https://doi.org/10.1016/j.fuel.2017.09.059.
[26] H. Boujjat, S. Rodat, S. Chuayboon, S. Abanades, Experimental and numerical study of a directly irradiated hybrid solar/combustion spouted bed reactor for continuous steam gasification of biomass, Energy. 189 (2019) 116118. https://doi.org/10.1016/j.energy.2019.116118.
[27] B.J. Hathaway, J.H. Davidson, Autothermal hybridization and controlled production of hydrogen-rich syngas in a molten salt solar gasifier, International Journal of Hydrogen Energy. 46 (2021) 15257–15267. https://doi.org/10.1016/j.ijhydene.2021.02.048.
[28] A. Curcio, S. Rodat, V. Vuillerme, S. Abanades, Experimental assessment of woody biomass gasification in a hybridized solar powered reactor featuring direct and indirect heating modes, International Journal of Hydrogen Energy. 46 (2021) 37192–37207. https://doi.org/10.1016/j.ijhydene.2021.09.008.
[29] A. Curcio, S. Rodat, V. Vuillerme, S. Abanades, Design and validation of reactant feeding control strategies for the solar-autothermal hybrid gasification of woody biomass, Energy. 254 (2022) 124481. https://doi.org/10.1016/j.energy.2022.124481.
[30] S.K. Bhatia, D.D. Perlmutter, A random pore model for fluid-solid reactions: I. Isothermal, kinetic control, AIChE J. 26 (1980) 379–386. https://doi.org/10.1002/aic.690260308.
[31] H. Boujjat, S. Rodat, S. Abanades, Solar-hybrid thermochemical gasification of wood particles and solid recovered fuel in a continuously-fed prototype reactor, Energies. 13 (2020) 5217. https://doi.org/10.3390/en13195217.
[32] C. Li, K. Suzuki, Tar property, analysis, reforming mechanism and model for biomass gasification—An overview, Renewable and Sustainable Energy Reviews. 13 (2009) 594–604. https://doi.org/10.1016/j.rser.2008.01.009.
[33] J. Billaud, Gazéification de la biomasse en réacteur à flux entrainé: études expérimentales et modélisation, (n.d.) 227.

[34] S. Kajitani, S. Hara, H. Matsuda, Gasification rate analysis of coal char with a pressurized drop tube furnace, (2002) 8.
[35] H.J. Jeong, D.K. Seo, J. Hwang, CFD modeling for coal size effect on coal gasification in a two-stage commercial entrained-bed gasifier with an improved char gasification model, Applied Energy. 123 (2014) 29–36. https://doi.org/10.1016/j.apenergy.2014.02.026.
[36] C. Di Blasi, Combustion and gasification rates of lignocellulosic chars, Progress in Energy and Combustion Science. 35 (2009) 121–140. https://doi.org/10.1016/j.pecs.2008.08.001.
[37] D.G. Goodwin, H.K. Moffat, I. Schoegl, R.L. Speth, B.W. Weber, Cantera: An object-oriented software toolkit for chemical kinetics, thermodynamics, and transport processes, (2022). https://www.cantera.org.
[38] S. Shabbar, I. Janajreh, Thermodynamic equilibrium analysis of coal gasification using Gibbs energy minimization method, Energy Conversion and Management. 65 (2013) 755–763. https://doi.org/10.1016/j.enconman.2012.02.032.
[39] J. McBride, S. Gordon, M.A. Reno, Coefficients for calculating thermodynamic and transport properties of individual species, 1993.
[40] G.P. Smith, D.M. Golden, M. Frenklach, N.W. Moriarty, B. Eiteneer, M. Goldenberg, C.T. Bowman, R.K. Hanson, S. Song, W.C. Gardiner, V.V. Lissianski, Z. Qin, GRI-Mech, (n.d.). http://www.me.berkeley.edu/gri_mech/.
[41] A. Muroyama, T. Shinn, R. Fales, P.G. Loutzenhiser, Modeling of a dynamically-controlled hybrid solar/autothermal steam gasification reactor, Energy Fuels. 28 (2014) 6520–6530. https://doi.org/10.1021/ef501535r.
[42] V.G. Lisienko, G.K. Malikov, A.A. Titaev, Simple approximation of total emissivity of CO2 − H2O mixture used in the zonal method of calculation of heat transfer by radiation, (n.d.) 4.
[43] H.C. Hottel, Radiant Heat Transmission, in: Hear Transmission, 3rd Edition, McGraw-Hill, New-York, 1954.
[44] R. Siegel, J.R. Howell, Thermal Radiation Heat Transfer, 3rd Edition, Hemisphere, Washington, D.C., 1992.
[45] G. Maag, Heat transfer model and scale-up of an entrained-flow solar reactor for the thermal decomposition of methane, International Journal of Hydrogen Energy. (2010) 10.
[46] Q. Bellouard, S. Rodat, S. Abanades, S. Ravel, P.-É. Frayssines, Design, simulation and experimental study of a directly-irradiated solar chemical reactor for hydrogen and syngas production from continuous solar-driven wood biomass gasification, International Journal of Hydrogen Energy. 44 (2019) 19193–19205. https://doi.org/10.1016/j.ijhydene.2018.04.147.
[47] Y.A. Cengel, Heat Transfer: A Practical Approach, 3rd Edition, 2002.
[48] N. Epstein, J.R. Grace, Spouted and Spout-Fluid Beds: Fundamentals and Applications, Cambridge University Press, 2001.
[49] J.J. More, B.S. Garbow, K.E. Hillstrom, User guide for MINPACK-1. [In FORTRAN], Argonne National Lab., IL (USA), 1980. doi:10.2172/6997568.